Applied Physics Letters

α-In_2Se_3 based ferroelectric-semiconductor metal junction for non-volatile memories

Cite as: Appl. Phys. Lett. **117**, 183504 (2020); https://doi.org/10.1063/5.0021395
Submitted: 09 July 2020 . Accepted: 21 October 2020 . Published Online: 05 November 2020

Atanu K. Saha, Mengwei Si, Peide D. Ye, and Sumeet K. Gupta

Applied Physics Letters ARTICLE scitation.org/journal/apl

α-In_2Se_3 based ferroelectric-semiconductor metal junction for non-volatile memories

Cite as: Appl. Phys. Lett. **117**, 183504 (2020); doi: 10.1063/5.0021395
Submitted: 9 July 2020 · Accepted: 21 October 2020 ·
Published Online: 5 November 2020

View Online Export Citation CrossMark

Atanu K. Saha,[1,a] Mengwei Si,[1,2] Peide D. Ye,[1,2] and Sumeet K. Gupta[1]

AFFILIATIONS

[1]School of Electrical and Computer Engineering, Purdue University, West Lafayette, Indiana 47907, USA
[2]Birck Nanotechnology Center, West Lafayette, Indiana 47907, USA

[a]Author to whom correspondence should be addressed: saha26@purdue.edu

ABSTRACT

In this work, we theoretically and experimentally investigate the working principle and nonvolatile memory (NVM) functionality of a 2D α-In_2Se_3-based ferroelectric-semiconductor-metal-junction (FeSMJ). First, we analyze the semiconducting and ferroelectric properties of the α-In_2Se_3 van der Waals (vdW) stack via experimental characterization and first-principles simulations. Then, we develop a FeSMJ device simulation framework by self-consistently solving the Landau–Ginzburg–Devonshire equation, Poisson's equation, and charge-transport equations. Based on the extracted Fe-semiconductor (FeS) parameters, our simulation results show good agreement with the experimental characteristics of our fabricated α-In_2Se_3-based FeSMJ. Our analysis suggests that the FeS polarization-dependent modulation of Schottky barrier heights of FeSMJ plays a key role in providing the NVM functionality. Besides, the appearance of mobile carriers in FeS due to its semiconducting properties leads to a non-uniform electric field. This further induces partial polarization switching in the FeS layers, resulting in asymmetry in the FeSMJ characteristics for positive and negative voltages. Moreover, we show that the thickness scaling of FeS leads to a reduction in read/write voltage and an increase in distinguishability. Array-level analysis of FeSMJ NVM suggests a lower read-time and read-write energy with respect to the HfO_2-based ferroelectric insulator tunnel junction.

Ferroelectric (Fe) materials have gained immense research interest for their applications in electronic[1–4] devices due to their electrically switchable spontaneous polarization and hysteretic characteristics. Fe materials with a high bandgap, called Fe-insulators, have been extensively investigated for versatile nonvolatile memory (NVM) devices, such as Fe-random-access-memory (Fe-RAM),[5] Fe-field-effect-transistors (Fe-FETs),[6,7] and Fe-tunnel-junctions (FTJs).[8–10] Unlike Fe-RAM and Fe-FETs, where the Fe layer acts as a capacitive element, the FTJ functionality depends on the tunneling current through the Fe layer. In the FTJ, the Fe layer is sandwiched between two different metal electrodes. Due to the different properties (e.g., the screening length) of the electrodes, the tunneling barrier height at the metal-Fe interface of the FTJ depends on the polarization (P) direction. Thus, the FTJ can exhibit P-dependent tunneling-resistance that facilitates the sensing of its P-state, leading to the design of a two-terminal NVM element.[8] However, as the dominant transport mechanism of the FTJ is direct tunneling, to obtain a desired current density for sufficient operational speed, the Fe-insulator thickness needs to be significantly low (<3 nm for HZO[9]). Unfortunately, with thickness scaling, the Fe-insulator P decreases,[9] which reduces the ratio of the tunneling-resistance[9] and, therefore, the distinguishability of the FTJ memory states decreases. In addition, most of the Fe-insulators (i.e., doped-HfO_2) comprise oxygen atoms and the dynamic change in oxygen vacancies can play a major role in their Fe characteristics.[11] Therefore, a decrease in ferroelectricity with scaling and issues related to oxygen vacancies lead to significant challenges in the design and implementation of FTJ-based NVMs.

Similar to the Fe-insulator, Fe material with a low bandgap called the Fe-semiconductor (FeS) also exhibits spontaneous P, which is switchable via the applied electric-field.[12–16] The van der Waals (vdW) stack of α-In_2Se_3 has recently been discovered as a 2D FeS material that can retain the Fe and semiconducting properties, even for a monolayer thickness.[12–16] This suggests a remarkable possibility for thickness scaling. In addition, as α-In_2Se_3 is not an oxide, the issues related to oxygen vacancies are expected to be non-existent in this FeS material. Recently, similar to the FTJ, a metal-FeS-metal junction device (called the FeSMJ) has been demonstrated to exhibit P-dependent resistance states.[17] Unlike the FTJ, the FeSMJ can provide significant current density even with a high FeS thickness and it does not require different metal electrodes for NVM functionalities.[17] To understand such a unique working principle of FeSMJs and to enable

their device-level optimization, a detailed analysis of the material properties of α-In_2Se_3 as well as the device characteristics is needed. To address this need, in this work, we experimentally and theoretically analyze α-In_2Se_3-based FeSMJ devices and examine their thickness scalability. Our analysis is based on experimental characterization, first-principles simulations, and self-consistent device simulation. Moreover, we investigate the FeSMJ thickness scalability and compare it with the FTJ at the device and array levels to analyze its potential for NVM applications.

To begin with, we first discuss the material properties of α-In_2Se_3. Unit cells of the α-In_2Se_3 monolayer are shown in Figs. 1(a)–1(d), indicating a non-centrosymmetric crystal structure, where the central Selenium (Se) atom is displaced from the centrosymmetric position. As a result, α-In_2Se_3 exhibits both in-plane [Figs. 1(a) and 1(b)] and out-of-plane polarization components [Figs. 1(c) and 1(d)]. The arrangement of α-In_2Se_3 layers in a vdW stack is shown in Fig. 1(e) where each layer is separated by a vdW gap.[12–14] Employing this α-In_2Se_3 as the FeS layer in a metal-FeS-metal configuration, the FeSMJ structure is shown in Fig. 1(e). Now, to characterize its properties, the α-In_2Se_3 vdW stack was grown by the melt method with a layered non-centrosymmetric rhombohedral R3m structure. The details of the fabrication process can be found in our previous work.[16] The high-angle-annular-dark-field STEM image of the thin α-In_2Se_3 flake is shown in Fig. 1(f), which signifies a high-quality single-crystalline hexagonal structure. The photoluminescence measurement [Fig. 1(g)] of α-In_2Se_3 suggests a direct optical/direct bandgap of ∼1.39 eV. To analyze the semiconducting properties further, we conduct first-principles simulations [based on density functional theory (DFT)] in Quantum Espresso (QE)[18,19] with hybrid orbital Heyd–Scuseria–Ernzerhof (HSE) correction.[20] Unlike previous simulation-based studies of a few numbers of layers,[12] we consider a bulk α-In_2Se_3 vdW stack by taking a supercell of three In_2Se_3 layers [Fig. 1(h)] periodically repeated in all three directions. Note that the thickness of our experimental sample is 120 nm (∼120 In_2Se_3 layers); therefore, we investigate the bulk properties, rather than a few-layer system. The simulated energy-dispersion relation is shown in Fig. 1(i), which illustrates a direct optical gap of ∼1.4 eV (consistent with experiments) and an indirect bandgap of ∼1.3 eV. The density of states (DOS) is shown in Fig. 1(j), which suggests a lower conduction DOS compared to the valence DOS. Hence, the equilibrium Fermi level (E_F) is closer to the conduction band minima (E_C) compared to the valence band maxima (E_V). We utilize these DOS characteristics in our device simulation for the calculation of the carrier concentration in the FeS layers, as discussed subsequently.

Next, we analyze the Fe properties of the α-In_2Se_3 vdW stack. Figure 2(a) shows the piezoresponse force microscopy (PFM) phase vs applied-voltage hysteresis loop of a 120 nm thick α-In_2Se_3 stack that suggests a Fe *P*-switching with a coercive voltage of ∼2 V. However, due to the semiconducting properties of α-In_2Se_3, a direct measurement of *P* through conventional methods is not possible.[16] Hence, we perform the Berry phase analysis[21] on the DFT wave-functions of α-In_2Se_3 in QE. Our analysis suggests an out-of-plane remanent *P* of ∼7.68 $\mu C/cm^2$. Note that, unlike previously calculated *P* (by the dipole correction method) for a few-layer system,[12] our calculated *P* is for bulk α-In_2Se_3. To further understand the Fe properties of α-In_2Se_3, the microscopic potential energy (averaged across the *x*-*y* plane) along the FeS thickness (z-axis) obtained from the DFT simulation is shown in Fig. 2(b). The extracted macroscopic potential [Fig. 2(c)] suggests an

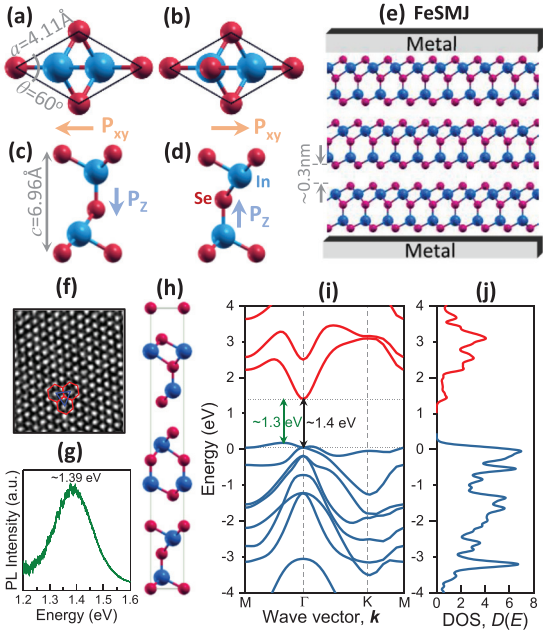

FIG. 1. Unit cell of α-In_2Se_3 (a) and (b) top view and (c) and (d) side view. (e) FeSMJ device structure with the vdW stack of α-In_2Se_3. (f) STEM image of the fabricated α-In_2Se_3 surface. (g) Measured photoluminescence (PL) spectrum. (h) Supercell of the bulk α-In_2Se_3 vdW stack. (i) Energy-dispersion relation and (j) density of states of the α-In_2Se_3 vdW stack from DFT simulation.

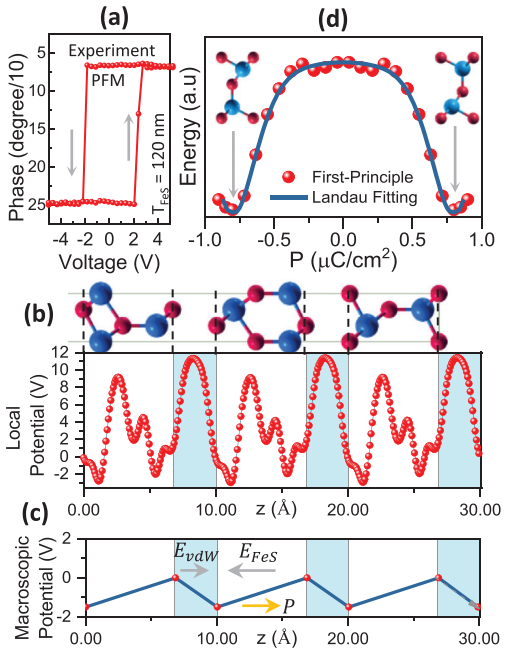

FIG. 2. (a) Measured PFM phase response of FeS with $T_{FeS} = 120$ nm. (b) Local electrostatic potential and (c) macroscopic potential profile in the α-In_2Se_3 vdW stack (along the z-axis). (d) Polarization vs energy of α-In_2Se_3.

opposite electric-field in FeS layers and vdW gaps. Now, the electrostatic condition at the interface of FeS and vdW gap can be written as

$$\epsilon_0 E_{vdW} = \epsilon_0 \epsilon_r E_{FeS} + P. \quad (1)$$

Here, E_{vdW} and E_{FeS} are the electric-fields in the vdW gap and FeS layer, respectively, ϵ_r is the relative background permittivity of the FeS layer, ϵ_0 is the vacuum permittivity, and P is the spontaneous polarization. The above equation suggests that E_{vdW} and E_{FeS} can be non-zero and hold the opposite sign if and only if the P is non-zero. This further confirms the existence of spontaneous P in the FeS layer. Using the calculated values of P, E_{vdW}, and E_{FeS}, we obtain $\epsilon_r = \sim 7$ from Eq. (1). Furthermore, we calculate the total energy (u) with respect to the change in P based on the nudge-elastic-band (NEB)[22] method in QE. The change in P is captured by moving the central Se atoms between two stable positions as shown in Fig. 2(d) followed by the Berry phase calculation for P. To capture the temperature effect in u, we have considered phonon-energy correction[23] for 300 K temperature (discussed in the supplementary material). The resultant u-P characteristics are shown in Fig. 2(d), signifying a double-well energy landscape. We fit the simulated u-P characteristics with Landau's free energy polynomial[24] as shown in Fig. 2(d) based on the following equation:

$$u = \frac{1}{2}\alpha P^2 + \frac{1}{4}\beta P^4 + \frac{1}{6}\gamma P^6 + \frac{1}{8}\delta P^8. \quad (2)$$

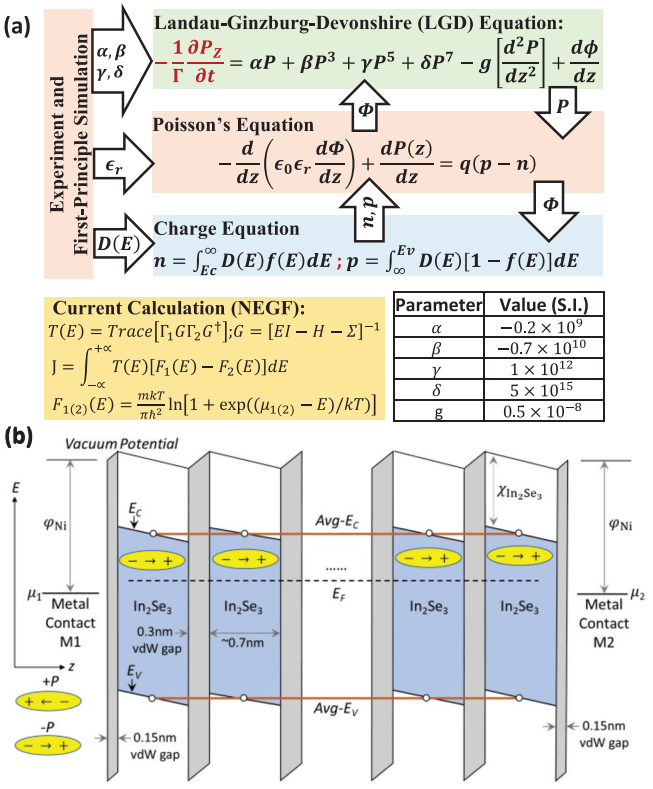

FIG. 3. (a) Self-consistent simulation flow, equations, and parameters used for FeSMJ device simulation. (b) Band alignment of the M-FeS-M structure before equilibrium.

The obtained Landau coefficients (α, β, γ, and δ) are shown in the inset of Fig. 3(a). Based on the extracted parameters of α-In_2Se_3, we self-consistently solve the Landau–Ginzburg–Devonshire equation,[3] Poisson's equation, and semiconductor charge equations for the FeSMJ structure. Then, we use the potential profile in a Non-Equilibrium Green's Function (NEGF) based transport solver to calculate the current in the FeSMJ. The simulation flow and parameters are shown in Fig. 3(a). In our simulation, we consider the vdW gap of 3 Å between the subsequent FeS layers (obtained from DFT simulation with structural relaxation) along with a vdW gap of 1.5 Å between the metal and FeS layer as shown in Fig. 3(b). We utilize this simulation framework along with the experimental results to investigate the FeSMJ device characteristics.

The top-view of the fabricated FeSMJ is shown in Fig. 4(a). Here, the FeS thickness (T_{FeS}) is 120 nm and the same metal (Ni) is used as the top and bottom contacts. The measured current (I) vs voltage (V) characteristics [Fig. 4(b)] exhibit a counterclockwise hysteresis due to which the FeSMJ shows two different resistive states. Let us define the current in the low-resistance state (LRS) and high-resistance state (HRS) as I_{LRS} and I_{HRS}, respectively. Note that the I_{HRS} to I_{LRS} switching occurs near ~2 V, which is similar to the coercive voltage of P-switching [see the PFM phase in Fig. 2(a)], indicating that the

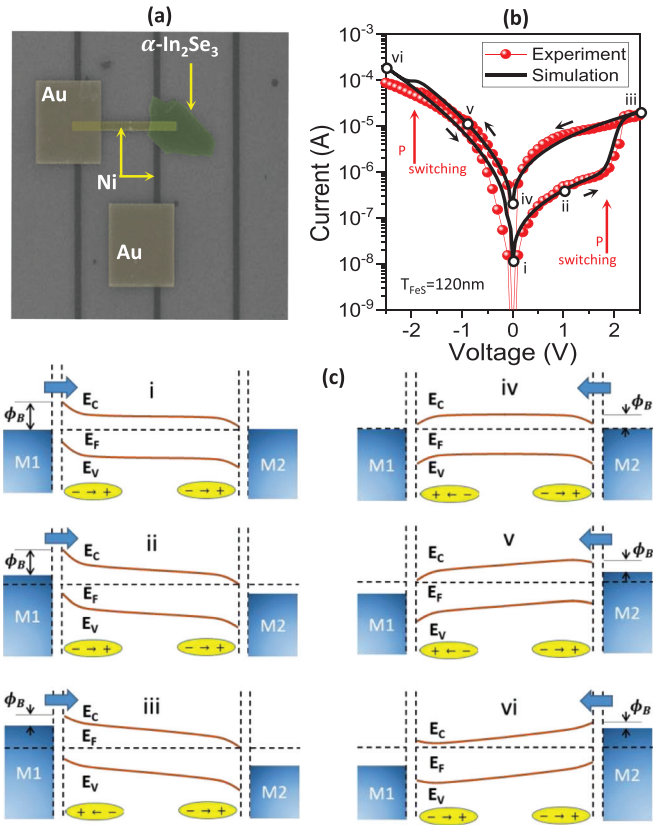

FIG. 4. (a) SEM image of the fabricated FeSMJ. (b) Measured and simulated I-V characteristics of the FeSMJ with $T_{FeS} = 120$ nm. (c) Band diagram of the FeSMJ for different points marked in (b). Here, E_C and E_V are taken at the center of each FeS layer and the vdW regions within the FeS layers are not shown for clarity.

change in current is due to the P-switching in the FeS layer. Here, one noticeable thing is that the characteristics are asymmetric with respect to the voltage polarity. For example, the hysteresis window, currents (I_{LRS} and I_{HRS}), and their ratio (I_{LRS}/I_{HRS}) are unequal for positive and negative V. To understand the possible origin of asymmetry and the FeSMJ operation, we perform device-level simulation. The simulated I–V curve considering $T_{FeS} = 120$ nm and Ni as metal contacts is shown in Fig. 4(b), indicating good agreement with the experimental results. Note that our fabricated device [Fig. 4(a)] has a higher back-metal-FeS interface area compared to the top metal-FeS interface area. Similarly, to compute the current in our simulation, a higher area is considered for the back-metal-FeS interface compared to the top-metal-FeS interface. Due to a Schottky barrier at the metal-FeS interface [Fig. 3(b)], the observed current is due to the electron injection from the metal to FeS via Schottky tunneling along with direct tunneling through the vdW gaps.

Now, to understand the working principle, the equilibrium band diagram of the FeSMJ (along the FeS thickness) is shown in Fig. 4(c-i). Note that the band diagram is for an undoped α-In_2Se_3 in which the E_F is closer to the E_C, as discussed before. Without any loss of generality, let us assume that initially, all the FeS layers are in the -z directed polarization state (-P). Let us call the left electrode M1 and right electrode M2. Now, the P-induced negative (positive) bound charges appear in the FeS near the M1 (M2) interface. The bound charges and the work function difference between the metal and FeS induce an E-field within the vdW gap and the FeS layers. As a result, holes (electrons) appear at the FeS-M1 (M2) interface to partially compensate the negative (positive) bound charges. Simultaneously, a built-in potential with opposite polarity appears across the two FeS-M junctions, yielding different Schottky barrier heights (ϕ_B) for the mobile-carriers. For example, in Fig. 4(c-i), ϕ_B at the FeS-M1 interface is higher than at the FeS-M2 interface due to the negative and positive voltage across the respective vdW gaps. Depending on whether the electron-injecting barrier exhibits low or high ϕ_B, the FeSMJ operates in the LRS or HRS. Moreover, voltage-driven P-switching can enable transitioning between the LRS and HRS and vice versa. To understand this, let us consider a positive bias at M2. Hence, the electron injection takes place from M1 to FeS. As the corresponding ϕ_B is high, the FeSMJ operates in the HRS. Concurrently, the hole (electron) concentration at the FeS-M1 (M2) interface increases. As the hole DOS is higher compared to the electron DOS, the increase in the hole concentration is higher compared to the electron concentration [Fig. 4(c-ii)]. This leads to a higher electric-field near the FeS-M1 interface compared to the FeS-M2 interface. At sufficiently high positive voltages [~2 V in Fig. 5(d-ii)], the electric-field near the FeS-M1 increases beyond the coercive field. Hence, a few layers near the M1 interface switch to $+P$ ($+z$ directed) as shown in Fig. 4(c-iii). Consequently, ϕ_B at the FeS-M1 interface significantly decreases, leading to an sharp increase in the current (LRS). The LRS operation continues even when the voltage is reduced to 0 due to P-retention. Now, when a negative voltage is applied at M2, the electron injects from M2 to FeS [Fig. 4(c-iv)]. As the corresponding ϕ_B is low, the FeSMJ continues to operate in the LRS. With a further increase in the negative polarity voltage, the electric-field near the M1-FeS interface switches the polarization back to $-P$ [Fig. 4(c-vi)]. This significantly reduces the E-field near the M1-FeS interface, the effect of which penetrates throughout the FeS including near the electron injecting electrode (FeS-M2 interface), which reduces the current. However, unlike $V > 0$V, where switching from the HRS to the LRS is sharp, here the change in current is gradual. This is because for $V > 0$V, the change in ϕ_B of the electron injecting junction (FeS-M1) is large due to P-switching near that interface. On the other hand, for $V < 0$V, the electron injecting ϕ_B does not change significantly as P-switching occurs on the other electrode. Therefore, the voltage hysteresis, I_{LRS}, I_{HRS}, and I_{LRS}/I_{HRS} are asymmetric with respect to the voltage polarity (i.e., lower for $V < 0$ than for $V > 0$). To complete the discussion, if the initial P is opposite ($+P$ for all the FeS layers), the I–V characteristics would be the opposite of what we discussed so far, i.e., a gradual HRS-to-LRS switching for $V > 0$V (for P-switching near the FeS-M2 interface causing a non-significant change in the electron injecting ϕ_B) and a sharp LRS-to-HRS switching for $V < 0$V (due to P-switching near the FeS-M2 interface causing a change in the electron injecting ϕ_B). This can be understood from the symmetry of the device structure and by considering the relative nature of the P direction and the polarity of the applied voltage.

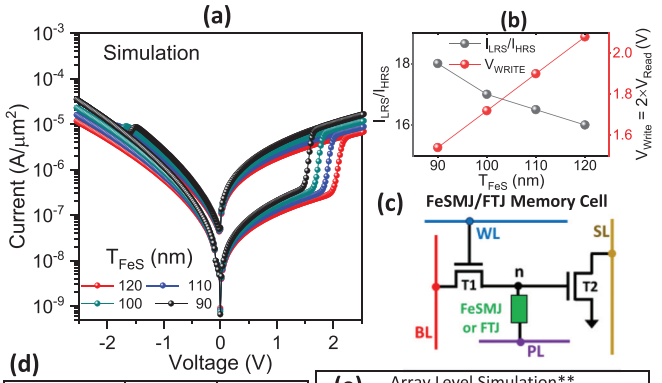

(d)

	FeSTJ	FTJ
Transport mechanism	Schottky tunneling	Direct tunneling
Current density	~10^{-5} A/μm^2	>10^{-8} A/μm^2
I_{LRS}/I_{HRS}	<10^3	<10^3

(e) Array Level Simulation**
Array Size = 1MB (1024x1024)

	FeSMJ	FTJ[25]	FTJ[26]	FTJ[27]	FTJ[28]
T_{READ}	0.6us	27us	94us	157us	292us
E_{READ}	1	16	73	125	221
E_{WRITE}	1	1.3	1.6	0.92	1.8

** In table-(e) the values are normalized with resect to the FeSMJ values.
Comparison is performed for iso-area and iso-sense-margin (SM = 15uA)

FIG. 5. (a) I–V characteristics, (b) write voltage, read voltage, and I_{LRS}/I_{HRS} of the FeSMJ for different FeS thicknesses. (c) FeSMJ/FTJ memory cell. (d) Device and (e) array level comparison between the FeSMJ and FTJ (T_{READ}: read time, E_{READ}: read energy, and E_{WRITE} = write energy).

Now, let us discuss the influence of the FeS thickness on FeSMJ device characteristics. The simulated I–V characteristics of the FeSMJ with different T_{FeS} are shown in Fig. 5(a). With thickness scaling, the coercive-field can be achieved at a lower applied voltage; therefore, the required voltage to switch the resistance state (called write voltage, V_{write}) decreases as shown in Fig. 5(b). Also, a decrease in T_{FeS} leads to an increase in the electric-field (for the same applied voltage), yielding an increase in both I_{LRS} and I_{HRS} as shown in Fig. 5(a). Note that the P-induced bound charges in the FeS-M interfaces lead to an E-field in the FeS layers (even in the absence of an applied voltage). Such an E-field further leads to a built-in potential across the FeS layers, where the built-in potential increases with the increase in the FeS thickness. Moreover, this built-in potential leads to mobile carrier density near

the M-FeS interface (as the local potential determines the difference between the Fermi level and conduction/valence-band). However, with the decrease in T_{FeS}, the built-in potential decreases and that leads to a lower mobile carrier concentration near the M-FeS interface. Now, recall that the mobile-carrier concentration in FeS partially compensates the effect of P-induced bound charge. As the mobile-carrier concentration decreases with the decrease in T_{FeS}, the effect of P-induced bound charge becomes more prominent. Hence, the P-dependent modulation in ϕ_B increases with the decrease in T_{FeS}, which leads to an increase in I_{LRS}/I_{HRS} [Fig. 5(b)]. Consequently, improved distinguishability (I_{LRS}/I_{HRS}) along with low voltage NVM operation can be achieved by scaling down the T_{FeS}.

Next, we evaluate the FeSMJ NVM performance in comparison with the FTJ. In an array, each NVM cells[25] [Fig. 5(c)] is composed of a FeSMJ/FTJ connected in series with an access-transistor (T1) and their internal node (n) is connected to the gate of another transistor (T2) that senses the FeSMJ/FTJ resistive state-dependent discharging of the internal node potential. The read and write methodologies of this 2 T-1R memory cell are described in the supplementary material. In this analysis, we compare the different flavors of HfO_2-based FTJs[25–28] with our FeSMJ devices for an array size of 1 Mb by considering iso-cell-area and iso-sense-margin (discussed in the supplementary material). The device-level comparison [Fig. 5(d)] suggests that the FeSMJ has a key advantage of higher current density than the HfO_2-based FTJ (due to Schottky transport in the former as opposed to direct tunneling in the latter). Therefore, for the same area, the FeSMJ provides lower resistance ($\sim 10^{-3}$ times) compared to the FTJs. As the discharging of the internal node (n) depends on the FeSMJ/FTJ resistance, the FeSMJ provides faster discharge and, hence, smaller read-time compared to FTJs [Fig. 5(e)]. Furthermore, due to the slow discharge of the internal node, the T2 transistor remains turned ON for a longer period of time for the FTJ. As a result, we observe significantly higher read energy for the FTJ compared to the FeSMJ. Moreover, we observe a little higher write energy for the FTJ[25,26,28] due to its higher write voltage (>3 V) compared to the FeSMJ (2.5 V). Due to such a notable benefit of the FeSMJ over HfO_2-based FTJs for NVM applications, further exploration of the FeSMJ is required to investigate its retention characteristics in addition to its correlation with scaling. Note that, in this comparison, we only consider HfO_2-based FTJs because of their aggressive scalability.[29] However, there are different perovskite-based FTJs (with significantly high current and high I_{LRS}/I_{HRS}) where the memory operation not only depends on the P-switching but also depends on the migration of oxygen vacancies,[30] ions,[31] and formation of the conductive paths.[32] The scalability and variability of such devices are yet to be investigated and, therefore, not included in this comparison.

In summary, the FeS polarization induces a built-in potential across the vdW gap between FeS and metal contact, leading to a P-dependent Schottky barrier for electron injection. By invoking voltage-driven P-switching, the barrier height can be modulated, which leads to transitions between the HRS and LRS in the FeSMJ. Furthermore, we show that the appearance of mobile-carriers in FeS can lead to a partial P-switching, yielding asymmetric I–V characteristics of FeSMJ. Also, with T_{FeS} scaling, I_{LRS}/I_{HRS} increases and read-write voltages decrease. Most importantly, the exhibits a significantly high current density due to Schottky tunneling. Due to such appealing characteristics and fundamental differences in the transport mechanisms, FeSMJ-NVM exhibits significantly improved performances compared to FTJ-NVM.

See the supplementary material for the phonon energy correction, NVM array design, layout design, and read-write schemes.

DATA AVAILABILITY

The data that support the findings of this study are available within this article and its supplementary material.

REFERENCES

[1] H. Mulaosmanovic, E. Chicca, M. Bertele, T. Mikolajickac, and S. Slesazecka, Nanoscale **10**, 21755 (2018).
[2] H. Mulaosmanovic, J. Ocker, S. Müller, M. Noack, J. Müller, P. Polakowski, T. Mikolajick, and S. Slesazeck, in Symposium on VLSI Technology (2017), pp. T176-T177.
[3] A. K. Saha and S. K. Gupta, Sci. Rep. **10**, 10207 (2020).
[4] Z. Tan, L. Hong, Z. Fan, J. Tian, L. Zhang, Y. Jiang, Z. Hou, D. Chen, M. Qin, M. Zeng, J. Gao, X. Lu, G. Zhou, X. Gao, and J.-M. Liu, NPG Asia Mater. **11**, 20 (2019).
[5] M. Park, Y. Lee, T. Mikolajick, U. Schroeder, and C. Hwang, MRS Commun. **8**(3), 795 (2018).
[6] K. Chatterjee, S. Kim, G. Karbasian, A. J. Tan, A. K. Yadav, A. I. Khan, C. Hu, and S. Salahuddin, IEEE Electron Device Lett. **38**, 1379 (2017).
[7] P. Sharma, K. Tapily, A. K. Saha, J. Zhang, A. Shaughnessy, A. Aziz, G. L. Snider, S. Gupta, R. D. Clark, and S. Datta, in Symposium on VLSI Technology (2017), pp. T154–T155.
[8] V. Garcia and M. Bibes, Nat. Commun. **5**, 4289 (2014).
[9] F. Mo, Y. Tagawa, T. Saraya, T. Hiramoto, and M. Kobayashi, in IEEE International Electron Device Meeting (IEDM) (2018), pp. 16.3.1–16.3.4.
[10] H. Ryu, H. Wu, F. Rao, and W. Zhu, Sci. Rep. **9**, 20383 (2019).
[11] D. Z. Gao, J. Strand, M. S. Munde, and A. L. Shluger, Front. Phys. **7**, 43 (2019).
[12] W. Ding, J. Jhu, Z. Wang, Y. Gao, D. Xiao, Y. Gu, Z. Zhang, and W. Zhu, Nat. Commun. **8**, 14956 (2017).
[13] C. Zheng, L. Yu, L. Zhu, J. L. Collins, D. Kim, Y. Lou, C. Xu, M. Li, Z. Wei, Y. Zhang, M. T. Edmonds, S. Li, J. Seidel, Y. Zhu, J. Z. Liu, W. Tang, and M. S. Fuhrer, Sci. Adv. **4**, eaar7720 (2018).
[14] C. Cui, W. Hu, X. Yan, C. Addiego, W. Gao, Y. Wang, Z. Wang, L. Li, Y. Cheng, P. Li, X. Zhang, H. N. Alshareef, T. Wu, W. Zhu, X. Pan, and L. Li, Nano Lett. **18**, 1253 (2018).
[15] S. Wan, Y. Li, W. Li, X. Mao, W. Zhu, and H. Zeng, Nanoscale **10**, 14885 (2018).
[16] M. Si, A. K. Saha, S. Gao, G. Qiu, J. Qin, Y. Duan, J. Jian, C. Niu, H. Wang, W. Wu, S. K. Gupta, and P. D. Ye, Nat. Electron. **2**, 580 (2019).
[17] M. Si, Y. Luo, W. Chung, H. Bae, D. Zheng, J. Li, J. Qin, G. Qiu, S. Yu, and P. D. Ye, in IEEE International Electron Device Meeting (IEDM) (2019).
[18] P. Giannozzi, S. Baroni, N. Bonini, M. Calandra, R. Car, C. Cavazzoni, D. Ceresoli, G. L. Chiarotti, M. Cococcioni, I. Dabo, A. Dal Corso, S. Fabris, G. Fratesi, S. de Gironcoli, R. Gebauer, U. Gerstmann, C. Gougoussis, A. Kokalj, M. Lazzeri, L. Martin-Samos, N. Marzari, F. Mauri, R. Mazzarello, S. Paolini, A. Pasquarello, L. Paulatto, C. Sbraccia, S. Scandolo, G. Sclauzero, A. P. Seitsonen, A. Smogunov, P. Umari, and R. M. Wentzcovitch, J. Phys.: Condens. Matter **21**, 395502 (2009).
[19] P. Giannozzi, O. Andreussi, T. Brumme, O. Bunau, M. Buongiorno Nardelli, M. Calandra, R. Car, C. Cavazzoni, D. Ceresoli, M. Cococcioni, N. Colonna, I. Carnimeo, A. Dal Corso, S. de Gironcoli, P. Delugas, R. A. DiStasio, Jr., A. Ferretti, A. Floris, G. Fratesi, G. Fugallo, R. Gebauer, U. Gerstmann, F. Giustino, T. Gorni, J. Jia, M. Kawamura, H.-Y. Ko, A. Kokalj, E. Küçükbenli, M. Lazzeri, M. Marsili, N. Marzari, F. Mauri, N. L. Nguyen, H.-V. Nguyen, A. Otero-de-la-Roza, L. Paulatto, S. Poncé, D. Rocca, R. Sabatini, B. Santra, M. Schlipf, A. P. Seitsonen, A. Smogunov, I. Timrov, T. Thonhauser, P. Umari, N. Vast, X. Wu, and S. Baroni, J. Phys.: Condens. Matter **29**, 465901 (2017).

[20]A. V. Krukau, O. A. Vydrov, A. F. Izmaylov, and G. E. Scuseria, J. Chem. Phys. **125**, 224106 (2006).
[21]R. D. King-Smith and D. Vanderbilt, Phys. Rev. B **47**, 1651 (1993).
[22]G. Henkelman, B. P. Uberuaga, and H. A. Jónsson, J. Chem. Phys. **113**, 9901 (2000).
[23]D. S. Sholl and J. A. Steckel, *Density Functional Theory: A Practical Introduction* (Wiley, 2009), pp. 113–130.
[24]L. D. Landau, in *Collected Papers of L. D. Landau*, edited by D. Ter Haar (Pergamon Press, 1965), pp. 193–216.
[25]S. Slesazeck, T. Ravsher, V. Havel, E. T. Breyer, H. Mulaosmanovic, and T. Mikolajick, in IEEE International Electron Device Meeting (IEDM) (2019), pp. 38.6.1–38.6.4.
[26]B. Max, M. Hoffmann, S. Slesazeck, and T. Mikolajick, in 48th European Solid-State Device Research Conference (ESSDERC) (2018).
[27]M. Kobayashi, Y. Tagawa, F. Mo, T. Saraya, and T. Hiramoto, IEEE J. Electron Devices Soc. **7**, 134–139 (2019).
[28]S. Fujii, Y. Kamimuta, T. Ino, Y. Nakasaki, R. Takaishi, and M. Saitoh, in Symposium on VLSI Technology (2016), pp. 1–2.
[29]H.-J. Lee, M. Lee, K. Lee, J. Jo, H. Yang, Y. Kim, S. Chul Chae, U. Waghmare, and J. H. Lee, Science **369**(6509), 1343–1347 (2020).
[30]P. Hou, J. Wang, X. Zhong, and Y. Wu, RSC Adv. **6**(59), 54113–54118 (2016).
[31]R. Guo, Y. Zhou, L. Wu, Z.-R. Wang, Z. Lim, X. Yan, W. Lin, H. Wang, H. Yoong, S. Chen, T. Venkatesan, J. Wang, G. M. Chow, A. Gruverman, X. Miao, Y. Zhu, and J. Chen, ACS Appl. Mater. Interfaces **10**(15), 12862–12869 (2018).
[32]H. Yamada, V. Garcia, S. Fusil, S. Boyn, M. Marinova, A. Gloter, S. Xavier, J. Grollier, E. Jacquet, C. Carrétéro, C. Deranlot, M. Bibes, and A. Barthélémy, ACS Nano **7**(6), 5385–5390 (2013).